

Research Article

Current-Sensorless Control Strategy for the MPPT of a PV Cell: An Energy-Based Approach

Hayden Phillips-Brenes ^{1,2}, Roberto Pereira-Arroyo ², Renato Rímolo-Donadío ^{1,2}
and Mauricio Muñoz-Arias ³

¹Doctorado en Ciencias Naturales Para el Desarrollo (DOCINADE), Instituto Tecnológico de Costa Rica, Universidad Nacional, Universidad Estatal a Distancia, Costa Rica

²Escuela de Ingeniería Electrónica, Instituto Tecnológico de Costa Rica, Costa Rica

³Faculty of Science and Engineering, University of Groningen, Netherlands

Correspondence should be addressed to Hayden Phillips-Brenes; hphillips@itcr.ac.cr, Roberto Pereira-Arroyo; rpereira@itcr.ac.cr, Renato Rímolo-Donadío; rrimolo@tec.ac.cr, and Mauricio Muñoz-Arias; m.munoz.arias@rug.nl

Received 15 May 2022; Revised 15 July 2022; Accepted 12 August 2022; Published 10 September 2022

Academic Editor: Mark van Der Auweraer

Copyright © 2022 Hayden Phillips-Brenes et al. This is an open access article distributed under the Creative Commons Attribution License, which permits unrestricted use, distribution, and reproduction in any medium, provided the original work is properly cited.

A novel energy-based modelling and control strategy is developed and implemented to solve the maximum power point tracking problem when a photovoltaic cell array is connected to consumption loads. A mathematical model that contains key characteristic parameters of an energy converter stage connected to a photovoltaic cell array is proposed and recast using the port-Hamiltonian framework. The system consists of input-output power port pairs and storage and dissipating elements. Then, a current-sensorless control loop for a maximum power point tracking is designed, acting over the energy converter stage and following an interconnection and damping assignment passivity-based strategy. The performance of the proposed strategy is compared to a (classical) sliding mode control law. Our energy-based strategy is implemented in a hardware platform with a sampling rate of 122 Hz, resulting in lower dynamic power consumption compared to other maximum power point tracking control strategies. Numerical simulations and experimental results validate the performance of the proposed energy-based modelling and the novel control law approach.

1. Introduction

The emerging advances in photovoltaic (PV) cell panel manufacturing processes have pushed forward the technology. It is considered a feasible option for energy production instead of fossil fuels due to its safe, sustainable, and clean supply capabilities. The feasibility is reflected in the advancement of installed solar capacity by at least ten times from 2010 to 2018 [1]. However, the current PV panel technology forfeits up to 25% of its generated energy due to a deficient performance and dependence on climatic conditions [2]. Thus, the maximum power point tracking (MPPT) problem should be addressed in order to enhance the PV cell arrays' energy generation. By having an adequate MPPT strategy, the power transfer efficiency from the PV cell arrays to consumption loads is improved. The MPPT focuses on

matching the PV panel's output load by controlling a DC voltage converter stage, ensuring the maximum power transfer [2–4].

Different approaches for the MPPT techniques based on application requirements and system constraints define the scope and objective of the control technique [5]. A first approach is focused on the *maximum power point (MPP) of a single stage of PV cells*, where the objective of the control is the extraction of the maximum power of a specific block of PV cells (or a single PV cell) of the whole array, under any environmental condition. The stage is generally governed by a control on a DC-DC converter from a microcontroller and works specifically over the block independently from the rest of the PV cell array [2, 6–16]. Since the objective of this strategy relies on the local control of the MPPT on a low area of PV cells, the robustness of the solution relies

on the control capability to reach the MPP under disturbances over the whole controlled stage, i.e., disturbances on radiation or output load. Consequently, the shading issue is neglected from our scope, and later improvements on the PV arrays could be required to cover shading issues for more extensive areas. Traditional methods, such as constant voltage tracking, open-circuit voltage tracking, short-circuit current tracking, lookup table, current scanning, and curve fitting, are recommended when addressing the shading issues. Although the effectiveness of intelligent control strategies such as genetic algorithms, fuzzy logic algorithms, artificial neural networks, and upgraded P&O has been verified by experiments in many cases, such algorithms still have the disadvantages of high complexity and slow convergence speed [13]. Furthermore, the local MPPT approach is helpful in applications such as space satellites, solar vehicles, and solar water-pump systems [4].

A second approach is focused on the *global MPP of the whole PV cell array* or a big block of the array, where partial shading (PS) has an appreciable effect due to the area of the array. The PS distorts the global MPPT of the PV cell array due to the reflection of the power-voltage characteristics of any single shaded stage of PV cells over the characteristics of the whole PV cell array. It results in multiple peaks that could distract the MPPT control unit, while it may remain into a local MPP instead of a global one; see for instance [3, 17–26]. These techniques attain a balance of the power distribution between shaded, partially shaded, and fully illuminated stages of PV cells over the area of the whole array. The strategy is based on the flexibility to modify the architecture of the array [3]. Intelligent techniques, such as fuzzy logic control, artificial neural networks, and particle swarm optimization, have the advantage of working with imprecise inputs, becoming more suitable methods for applications where PS is a critical issue [5].

Robust controllers have been previously proposed to improve the performance of the PV cell arrays on the local MPP. For example, the sliding mode controller (SMC) represents a robust algorithm that efficiently responds to environmental changes and load variations, [7, 8, 19, 27]. The stability and robustness of the SMC have been verified through simulations and experiments, reported in [7, 8, 19, 28]. The SMC nonlinear control strategy proposes differential mapping algorithms that require constant and simultaneous sensing of voltage and current at the output of the PV cell array to perform the MPPT, [9, 20]. Such a nonlinear strategy includes extra steps to determine future states from previous ones based on historical data [7, 19].

On the other hand, in [10], an interconnection and damping assignment passivity-based control (IDA-PBC) is proposed to address the local MPPT problem. Their IDA-PBC method provides a strategy that brings the system to the desired energy equilibrium by sensing the instantaneous current/voltage responses from the PV cell, avoiding the estimation of future and past states.

The strategies mentioned above, based on “electrical current monitoring”, presents several inconveniences thoroughly discussed in [29, 30]. Examples of such inconveniences are the loss of connections, replacement complexity,

inconsistent sensibility and resolution at low current, parasitic magnetic energy remanence in the cores, periodical calibration requirements, and erratic frequency responses. Moreover, external current sensors are usually expensive, which increases the inherent cost of the PV power system [11, 29, 31]. Finally, implementing algorithms of future-step prediction required a higher operating frequency and memory from the controller.

Consequently, the elimination of current sensors to track the MPP has been proposed as a counterpart to increase the cost benefits of PV systems [31]. Previous surveys have classified the so-called current-sensorless techniques according to their features and type of MPPT control strategies. See, for instance, [4, 5, 31] and the references therein. Specifically, the temperature/radiation monitoring (TRM) technique demonstrates a lower dependency on the topology and direct sensing connections. Controllers based on sensing radiation are seen as a more effective solution due to their economic advantage, fast response, and noninvasive characteristics [4]. Hence, the radiation parameter might be familiar to any PV cell connected to the same array, allowing a single sensor for control purposes.

In this paper, we propose an energy-based modelling approach for a PV cell array system connected to a DC-DC boost converter, based on the port-Hamiltonian formalism of [32–34]. The formalism is adopted here since the system has energy storage and dissipating elements (inter-connected with input-output power port-pairs). The port-Hamiltonian framework is the natural selection modelling approach because it allows a clear physical interpretation of the system’s energy flow towards a robust and scalable control design. Thus, inspired by [35, 36], a novel current-sensorless control algorithm in the framework of an IDA-PBC strategy is able to track the local MPP under variations of solar irradiance and output loads. The inputs for the control are the output voltage of the PV cell array and the sensed solar irradiance. The control objective is reached by setting the impedance matching between two stages: the PV cell array and a DC-DC boost converter system.

Since the control is based on sensing irradiation as a control input, the strategy allows connecting several PV cell stages to the same irradiation sensor with a separated control per stage. Our proposed strategy is effective since it ensures the extraction of the maximum power from any PV cell or stage. Nonetheless, the strategy requires that environmental conditions and disturbances remain homogeneously over the PV cell stages interconnected to the same radiation sensor. Furthermore, the proposed strategy demands lower frequency and power consumption than other robust control laws such as the SMC strategy, requiring noncomplex hardware to implement the control algorithm. The controller could be extended to several independent MPPT stages interconnected to a single solar irradiance sensor, decreasing the cost of sensing devices. Such an extension implementation is left out of the current work. The outline of this paper is as follows. Section 2 recapitulates the port-Hamiltonian modelling framework. In the same section, we summarize the IDA-PBC technique of [35, 36] and the SMC strategy of [8, 12]. In Section 3, we have proposed a novel port-

Hamiltonian modelling approach for the PV cell array connected to a solar irradiance sensor and a DC-DC boost converter system. From our port-Hamiltonian modelling approach, we have developed a sensorless control loop in Section 4, ruled by a control algorithm designed under the IDA-PBC strategy, that avoids the current monitoring as in [10]. Furthermore, in Section 5, simulation results are given to demonstrate the performance of the proposed IDA-PBC compared to the SMC. The system is characterized, implemented, and controlled with a noncomplex hardware platform, and the experimental results are presented in Section 6. Finally, in Section 7 key concluding remarks and future work are provided.

2. Mathematical Modelling and Control Strategies

Firstly, it is necessary to cover the bases of the port-Hamiltonian modelling framework, as a preamble to develop a useful mathematical model to design a IDA-PBC strategy, for a further comparison with the well-known SMC strategy.

Notation 1. The time differential and the gradient of a scalar vector are given by

$$\dot{x} \frac{dx}{dt}, \nabla_x \frac{\delta}{\delta x}. \quad (1)$$

Furthermore, all vectors are considered as column vectors.

2.1. Port-Hamiltonian Framework. We first recapitulate the port-Hamiltonian (pH) framework for a general class of (non)linear physical systems, which is based on the description of their energy (Hamiltonian) function, interconnection structure, dissipating elements, and power port pairs (inputs and outputs) [32–34]. A characteristic of the pH framework is how the energy transfer between the physical system and the environment is modelled via the energy storage and dissipation elements together with their power preserving ports [34].

A time-invariant pH system corresponds to the

$$\Sigma_{\text{pH}} \begin{cases} \dot{x} = [\mathcal{F}(x) - \mathcal{R}(x)] \nabla_x H(x) + g(x)u, \\ y = g(x)^T \nabla_x H(x), \end{cases} \quad (2)$$

where the state variable is given by $x \in \mathbb{R}^{\mathcal{N}}$, and the input-output port pair $\{u, y\}$ representing flows and efforts are

$$u \in \mathbb{R}^{\mathcal{M}}, y \in \mathbb{R}^{\mathcal{M}}. \quad (3)$$

Furthermore, the input, interconnection, and dissipation matrices of (2) are defined as

$$g(x) \in \mathbb{R}^{\mathcal{N} \times \mathcal{M}}, \quad (4)$$

$$\mathcal{F}(x) = -\mathcal{F}(x)^T, \mathcal{F}(x) \in \mathbb{R}^{\mathcal{N} \times \mathcal{N}}, \quad (5)$$

$$\mathcal{R}(x) = \mathcal{R}(x)^T \mu 0, \mathcal{R}(x) \in \mathbb{R}^{\mathcal{N} \times \mathcal{N}}, \quad (6)$$

where $\mathcal{M} \leq \mathcal{N}$ being $\mathcal{M} = \mathcal{N}$ a fully actuated system, and $\mathcal{M} < \mathcal{N}$ an under-actuated one for the example of mechanical systems. It follows that the energy function of the system (2) is

$$H(x) \in \mathbb{R}. \quad (7)$$

If (7) is differentiated with respect to time, meaning obtaining the Hamiltonian function along the trajectories of \dot{x} as in (2), it follows that

$$\begin{aligned} \dot{H}(x) &= \nabla_x^T H(x) \dot{x} \\ &= \nabla_x^T H(x) [\mathcal{F}(x) - \mathcal{R}(x)] \nabla_x H(x) + \nabla_x^T H(x) g(x)u \end{aligned} \quad (8)$$

$$\begin{aligned} &= \nabla_x^T H(x) \mathcal{F}(x) \nabla_x H(x) - \nabla_x^T H(x) \mathcal{R}(x) \nabla_x H(x) \\ &\quad + \nabla_x^T H(x) g(x)u, \end{aligned} \quad (9)$$

and since $\mathcal{F}(x)$ as in (5) is skew-symmetric, then $\nabla_x^T H(x) \mathcal{F}(x) \nabla_x H(x) = 0$. In addition to that, the matrix $\mathcal{R}(x)$ as in (6) is positive semi-definite, then $\nabla_x^T H(x) \mathcal{R}(x) \nabla_x H(x) \geq 0$, and since the output is $y = g(x)^T \nabla_x H(x)$ as in (2), hence, the power balance $\dot{H}(x)$ in (9) is reduced to

$$\dot{H}(x) = -\nabla_x^T H(x) \mathcal{R}(x) \nabla_x H(x) + y^T u \leq y^T u, \quad (10)$$

where we clearly see how system (2) would be conservative if $\dot{H}(x) = y^T u$ (dissipation matrix $\mathcal{R}(x) = 0$), and dissipative if $\dot{H}(x) < y^T u$ (dissipation matrix $\mathcal{R}(x) > 0$).

Next, we recapitulate the main control strategy developed to our PV cell and DC-DC boost converter system based on passivity.

2.2. Interconnection and Damping Assignment Passivity-Based Control (IDA-PBC). The IDA-PBC strategy is a well-established technique that has demonstrated high efficiency and robustness for the control design of nonlinear systems. The strategy was firstly described in the Euler-Lagrange equations of motion and, more recently, extended to the pH approach, as seen in [35–37]. Generally speaking, IDA-PBC focuses on changing the potential energy shape by employing a closed-loop energy function equal to the difference between the energy of the system and the energy supplied by the controller. The energy shaping is performed while the interconnecting and structural properties of the system are preserved. Therefore, the system reaches its equilibrium point through energy stabilization [35–37]. The system structure is transformed to obtain the new desired interconnection and damping matrices with key parameters obtained from solving a *partial differential equation* (PDE). The solution of the PDE characterizes all the energy functions that can be assigned [33, 36, 37]. Finally, one of the solutions is chosen such that minimum requirements are satisfied by which the static state feedback control function u in (2) is obtained. The feedback control renders a

closed-loop dynamics with a structured preserved pH system with dissipation. The proposed fully controlled system and the statements to satisfy the mathematical coherence of the structure are described in the following proposition.

Proposition 2 (see [36]). *Assuming the functions $\beta(x)$, $\mathcal{F}_a(x)$, $\mathcal{R}_a(x)$, and a vector function $\mathcal{H}(x)$ that satisfy*

$$\begin{aligned} & \{[\mathcal{F}(x, \beta(x)) + \mathcal{F}_a(x)] - [\mathcal{R}(x) + \mathcal{R}_a(x)]\} \mathcal{H}(x) \\ & = -[\mathcal{F}_a(x) - \mathcal{R}_a(x)] \nabla_x H(x) + g(x, \beta(x)), \end{aligned} \quad (11)$$

such that the new desired matrices $\mathcal{F}_d(x)$ and $\mathcal{R}_d(x)$ are defined as

$$\begin{aligned} \mathcal{F}_d(x) & := \mathcal{F}(x, \beta(x)) + \mathcal{F}_a(x), \\ \mathcal{R}_d(x) & := \mathcal{R}(x) + \mathcal{R}_a(x), \end{aligned} \quad (12)$$

in order to obtain a closed-loop system of the form

$$\dot{x} = [\mathcal{F}_d(x) - \mathcal{R}_d(x)] \nabla_x H_d(x). \quad (13)$$

It follows that the vector function $\mathcal{H}(x)$ should be found in order to obtain a controller function $\beta(x)$.

In order to preserve the pH structure of the closed loop in (13), a structure preservation of the matrix properties must be satisfied. Furthermore, the vector function $\mathcal{H}(x)$ should meet with a transpose property of its differential expression, known as integrability statement where the control function $\beta(x)$ can be obtained. Consequently, the stability conditions for the control function are defined from an equilibrium assignment and a Lyapunov stability analysis. Based on [35], each statement is mathematically described as

(i) Structure preservation

$$\mathcal{F}_d = -[\mathcal{F}_d]^T, \mathcal{R}_d = [\mathcal{R}_d]^T \mu 0. \quad (14)$$

(ii) Integrability

$$\nabla_x \mathcal{H}(x) = \nabla_x^T \mathcal{H}(x). \quad (15)$$

(iii) Equilibrium assignment (where x^* : state values at (locally) stable equilibrium)

$$\mathcal{H}(x^*) = -\nabla_x \mathcal{H}(x^*). \quad (16)$$

(iv) Lyapunov stability

$$\nabla_x \mathcal{H}(x^*) > -\nabla_x^2 \mathcal{H}(x^*). \quad (17)$$

Once having introduced the IDA-PBC design strategy, it follows in the next section the recapitulation of the well-known sliding mode control of [8, 12] which is applied to achieve stabilization of nonlinear systems.

2.3. Sliding Mode Control (SMC). The SMC strategy considers the dynamics of the solar irradiance sensor DC-DC transfer system and the output load. It consists of two operation modes. The first one is the approach mode, where the states of the system converge to a predefined domain known as the finite time *sliding function* σ_1 . The second one is the so-called *sliding mode* σ_2 , where the state of the system is restricted to a *sliding surface* that approaches the origin of the system, as in [7, 8, 12].

Given the electrical power supplied by the PV cell system, i.e., P_{pv} , and its output voltage v_{pv} to be defined later on, then the partial derivative $\nabla_{v_{pv}} P_{pv} = 0$ is selected as the sliding surface for the MPPT objective, such that the states of the system persistently approach maximum power transference. It follows that the *sliding surface* can be defined as

$$\nabla_{v_{pv}} P_{pv} = v_{pv} \left(\nabla_{v_{pv}} i_{pv} + \frac{i_{pv}}{v_{pv}} \right). \quad (18)$$

The assumption in (17) allows us to define the sliding mode σ_2 as

$$\sigma_2(t, x) = \nabla_{v_{pv}} i_{pv} + \frac{i_{pv}}{v_{pv}}. \quad (19)$$

with the system dynamics \dot{x} defined as

$$\dot{x} = \mathcal{F}(x) + \mathcal{G}(x) \sigma_1, \quad (20)$$

and where the *sliding function* σ_1 is obtained by solving the PDE

$$\dot{\sigma}_1 = [\nabla_x \sigma_1]^T \dot{x} = 0. \quad (21)$$

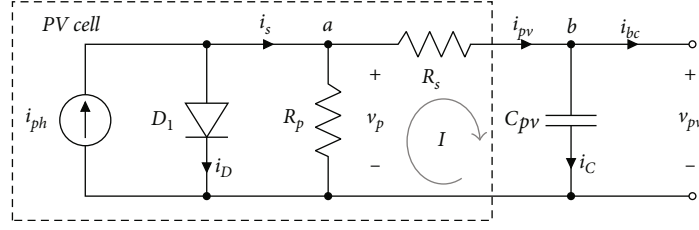
We now assume here that $[\partial \sigma / \partial x]^T$ is a reversible matrix, similarly to [12], such that the solution of (20) is given by

$$\sigma_1 = -\frac{[\nabla_x \sigma_1]^T \mathcal{F}(x)}{[\nabla_x \sigma_1]^T \mathcal{G}(x)} = 1 - \frac{v_{pv}}{v_L}. \quad (22)$$

then, the sliding function σ_1 should be solved to obtain the approach mode and complete the control algorithm for the controller. Finally, a *switch control* signal S_{SM} (from the SMC strategy) as a nonlinear input signal such that the controller is able to reach a duty cycle range is proposed. The form of S_{SM} is

$$S_{SM} = \begin{cases} 1 & \text{for } \sigma_1 + k\sigma_2 \geq 1 \\ \sigma_1 + k\sigma_2 & \text{for } 0 < \sigma_1 + k\sigma_2 < 1 \\ 0 & \text{for } \sigma_1 + k\sigma_2 \leq 0, \end{cases} \quad (23)$$

where k represents a positive scaling constant to be adjusted during the control design and implementation. The control signal S_{SM} in (22) is similar to the one proposed by [12].

FIGURE 1: Electric diagram of the PV cell with DC-link capacitor C_{pv} .

In the next section, the system of the PV cell connected to the DC-DC boost converter has been described following the pH framework.

3. A Port-Hamiltonian Modelling Approach to a PV Cell Connected to a DC-DC Boost Converter System

We first defined a pH approach to the PV cell modelling problem. Such an energy-based modelling strategy is previously introduced in [38] where we have proposed a model of a pumped hydro storage system powered by solar radiation. Also, in [38] we have simulated the system's open-loop model in order to evaluate its performance where a control strategy is not yet designed and implemented to attain MPPT. Instead, in [38] we have applied a conveniently fixed frequency square signal to activate the switch of the DC-DC *buck* converter system.

3.1. PV Cell Modelling Approach. The equivalent circuit of the PV stage shown in Figure 1 is based on the model of [39–41]. The PV cell electrical performance follows the *five-parameter model* approach as in [42–44]. Into the PV cell structure represented by the dashed rectangle, the current i_{ph} is generated by the solar irradiance, while the diode D_1 represents the equivalent model of the *p-n* join semiconductor layers. Furthermore, an equivalent resistor R_p is connected in a shunt configuration, followed by a serial resistor R_s at the system's output power. Meanwhile, the output of the the PV cell is linked to the next stage across the DC-link capacitor C_{pv} .

Based on the modelling approach of [42–44], the inner current i_s of the PV cell is defined as

$$i_s = i_{ph} - i_D, \quad (24)$$

In (23), the photogenerated current, i.e., i_{ph} , is given by

$$i_{ph} = (I_{SC,nom} + K_0(T - T_v)) \frac{G_{Sun}}{G_{nom}}, \quad (25)$$

where G_{Sun} represents the solar irradiance, G_{nom} the reference irradiance given by the manufacturer, $I_{SC,nom}$ the PV cell output short circuit measured at G_{nom} , K_0 the thermal correction factor, T the environment temperature, and T_v

the PV cell temperature. The current across the diode i_D in (23) is described by

$$i_D = i_0 \left(\exp \left(\frac{v_p}{nV_t} \right) - 1 \right), \quad (26)$$

where n is the diode quality factor and V_t the thermal voltage of the silicon layer junction. The saturation current i_0 in (25) is described by

$$i_0 = i_\alpha \left(\frac{T}{T_v} \right)^{3/n} \exp \left(\frac{-V_g}{nk} \left(\frac{1}{T} - \frac{1}{T_v} \right) \right), \quad (27)$$

where V_g is the silicium band gap, k the Boltzmann constant, and the constant i_α in (26) given by

$$i_\alpha = \frac{I_{SC,nom}}{\exp(V_{OC,nom}/nV_t) - 1}, \quad (28)$$

where $V_{OC,nom}$ is finally the PV cell open circuit voltage. The parameters and variables in (24), (25), (26), and (27) are fully explained in [43]. To determine the system's dynamics, we first consider Kirchhoff's current law on node a . The resulting equation is

$$i_{pv} = i_s - \frac{v_p}{R_p}. \quad (29)$$

Moreover, Kirchhoff's voltage law on the close path I yields

$$v_p = v_{pv} + R_s i_{pv}. \quad (30)$$

We substitute now (29) in (28) such that

$$i_{pv} = i_s - \frac{v_{pv}}{R_p} - \frac{R_s}{R_p} i_{pv}, = \frac{R_p}{R_p + R_s} i_s - \frac{1}{R_p + R_s} v_{pv}. \quad (31)$$

Furthermore, from the circuit's node b , we know that

$$i_C = i_{pv} - i_{bc}, \quad (32)$$

$$C_{pv} \dot{v}_{pv} = i_{pv} - i_{bc}. \quad (33)$$

If we define the electrical charge q_{pv} as a state variable in terms of the PV cell output voltage v_{pv} and the capacitor C_{pv}

such that $q_{pv} = C_{pv}v_{pv}$, then (32) could be rewritten in terms of (30). Finally, the resulting dynamics of the electrical charge is

$$\dot{q}_{pv} = -\frac{1}{R_p + R_s} \frac{q_{pv}}{C_{pv}} + \frac{R_p}{R_p + R_s} i_s - i_{bc}. \quad (34)$$

We realize now the dynamics of the system's second state variable that represents the electrical *flux*, i.e., ϕ_{pv} , which is given by

$$\dot{\phi}_{pv} = \frac{q_{pv}}{C_{pv}}. \quad (35)$$

Since the charge ϕ_{pv} in the capacitor C_{pv} is the only energy-storing element of the system in Figure 1, then the Hamiltonian function $H_{pv}(q_{pv}, \phi_{pv})$ of the PV cell stage is

$$H_{pv}(q_{pv}, \phi_{pv}) = \frac{1}{2C_{pv}} q_{pv}^2. \quad (36)$$

Thus, the partial derivatives of the Hamiltonian function in terms of the state variables q_{pv} and ϕ_{pv} are

$$\nabla_{q_{pv}} H_{pv}(q_{pv}, \phi_{pv}) = \frac{q_{pv}}{C_{pv}}, \quad (37)$$

$$\nabla_{\phi_{pv}} H_{pv}(q_{pv}, \phi_{pv}) = 0, \quad (38)$$

which means that the dynamics in (33) can be rewritten in terms of $\nabla_{q_{pv}} H_{pv}$ and $\nabla_{\phi_{pv}} H_{pv}$ as

$$\dot{q}_{pv} = -\frac{1}{R_p + R_s} \nabla_{q_{pv}} H_{pv} + k \nabla_{\phi_{pv}} H_{pv} + \frac{R_p}{R_p + R_s} i_s - i_{bc}, \quad (39)$$

with k being conveniently chosen as $k = -1$ to keep the *skew-symmetric* properties of a new $\mathcal{F}(x_{pv})$ matrix to be defined later on. In (38), we have left out the arguments of H_{pv} for notation simplicity.

The dynamics in (38) and (34), together with the energy function (35), are used to formulate the pH system Σ_{pv} of the PV cell, given by

$$\Sigma_{pv} \left\{ \begin{array}{l} \underbrace{\begin{bmatrix} \dot{q}_{pv} \\ \dot{\phi}_{pv} \end{bmatrix}}_{\dot{x}_{pv}} = \underbrace{\begin{bmatrix} -\frac{1}{R_p + R_s} & -1 \\ 1 & 0 \end{bmatrix}}_{\mathcal{F}(x_{pv}) - \mathcal{R}(x_{pv})} \underbrace{\begin{bmatrix} \nabla_{q_{pv}} H_{pv} \\ \nabla_{\phi_{pv}} H_{pv} \end{bmatrix}}_{\nabla_{x_{pv}} H_{pv}} + \underbrace{\begin{bmatrix} \frac{R_p}{R_p + R_s} \\ 0 \end{bmatrix}}_{g(x_{pv})} i_s - \begin{bmatrix} 1 \\ 0 \end{bmatrix} i_{bc}, \\ y_{pv} = g^T(x_{pv}) \nabla_{x_{pv}} H_{pv} = v_p. \end{array} \right. \quad (40)$$

where $\mathcal{R}(x_{pv}) = \text{diag}((1/R_p + R_s), 0)$, and $\mathcal{F}_{x_{pv}}$ is a skew-symmetric matrix with the form

$$\mathcal{F}_{x_{pv}} = \begin{bmatrix} 0 & -1 \\ 1 & 0 \end{bmatrix}. \quad (41)$$

Based on the dynamics of (39) with an input-output port pair $(u_{pv}, y_{pv}) = (i_s, v_p)$ and the Hamiltonian (35), and since $R_p + R_s \geq 0$, we see how the power balance (9) clearly holds.

For control design purposes, it is now necessary to find an expression to track the amplitude of v_{pv} according to the solar irradiance in order to obtain the so-called *current-sensorless* control strategy. Such expression is developed in the following subsection.

3.2. Equilibrium Trajectory of the PV Cell State Variables over the MPP. Since the transfer function of i_{pv} vs v_{pv} depends on the amplitude of the input current i_{ph} as in (24), thus the MPP is attained. The relationship between

i_{ph} and the MPP at the PV cell output in Figure 1 is given in terms of the output power $P_{out}(v_{pv})$ such that

$$\nabla_{v_{pv}} P_{out}(v_{pv}^*) = \nabla_{v_{pv}} (i_{pv} v_{pv}) \Big|_{v_{pv}^*} = 0, \quad (42)$$

$$\nabla_{v_{pv}} \left(\left(i_{ph} - i_0 \left(\exp \left(\frac{v_p}{nV_t} \right) - 1 \right) - \frac{v_p}{R_p} \right) v_{pv} \right) \Big|_{v_{pv}^*} = 0, \quad (43)$$

where $v_p = v_{pv} + i_{pv} R_s$, and v_{pv}^* is defined as the desired state of the PV cell voltage at the MPP. Furthermore, the resistance R_s is considered very low compared to R_p , resulting in $R_s \approx 0$. Assuming also i_0 constant, thus (42) becomes

$$i_{ph} + i_0 - i_0 \exp \left(\frac{v_{pv}^*}{nV_t} \right) - v_{pv}^* \left(\frac{2}{R_p} + \frac{i_0 \exp \left(\frac{v_{pv}^*}{nV_t} \right)}{nV_t} \right) \approx 0, \quad (44)$$

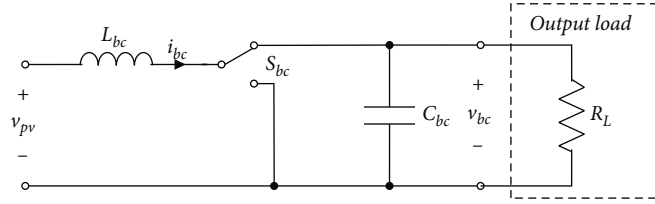


FIGURE 2: A DC-DC boost converter equivalent electric circuit.

where v_{pv}^* can be solved in terms of the input current i_{ph} by numerical methods, i.e., the so-called *equilibrium trajectory*. Finally, we see how the solar irradiance G_{Sun} as in (24) influences directly the current i_{ph} , which in turn also affects the desired PV cell voltage v_{pv}^* in (43).

The following section presents the mathematical modelling approach to the DC-DC boost converter stage under the pH framework. Such a stage has been interconnected with the PV cell subsystem in Section 3.4.

3.3. DC-DC Boost Converter Modelling Approach. A boost configuration is selected here to achieve a DC-DC voltage step-up conversion which is regulated by a switching device. The converter is able to draw the MPP from the PV cell by adjusting its duty cycle for given solar radiance levels. For further details regarding the working principles of the model, we refer to [45, 46] and the references therein.

Consider now the DC-DC boost converter configuration circuit shown in Figure 2. v_{pv} at the left side of the circuit represents the PV cell output voltage, and R_L at the right side represents a resistive output load connected to the PV cell via the DC-DC boost converter. Based on [8, 12], the system can be described by the dynamics of i_{bc} and v_{bc} . In addition to this, we define a two state switching device represented by $S_{bc} = \{0, 1\}$. Following the Biot-Savart Law, the dynamics of i_{bc} and v_{bc} are given in terms of the state variables $\phi_{bc} = L_{bc}i_{bc}$ (magnetic flux in the inductor) and $q_{bc} = C_{bc}v_{bc}$ (charge in the capacitor), respectively. By Kirchhoff's Laws, it follows that

$$\dot{q}_{bc} = -\frac{1}{R_L} \frac{q_{bc}}{C_{bc}} + S_{bc} \frac{\phi_{bc}}{L_{bc}}, \quad (45)$$

$$\dot{\phi}_{bc} = -S_{bc} \frac{q_{bc}}{C_{bc}} + v_{pv}. \quad (46)$$

We now define the Hamiltonian function $H_{bc}(q_{bc}, \phi_{bc})$ of the DC-DC boost converter in Figure 2 as

$$H_{bc}(q_{bc}, \phi_{bc}) = \frac{1}{2C_{bc}} q_{bc}^2 + \frac{1}{2L_{bc}} \phi_{bc}^2, \quad (47)$$

where, together with the dynamics of (44) and (45), we formulate the pH system Σ_{BC} of the boost DC-DC converter with an output load as

$$\Sigma_{BC} \begin{cases} \underbrace{\begin{bmatrix} \dot{q}_{bc} \\ \dot{\phi}_{bc} \end{bmatrix}}_{\dot{x}_{bc}} = \underbrace{\begin{bmatrix} -\frac{1}{R_L} & S_{bc} \\ -S_{bc} & 0 \end{bmatrix}}_{\mathcal{F}(x_{bc}) - \mathcal{R}(x_{bc})} \underbrace{\begin{bmatrix} \nabla_{q_{bc}} H_{bc} \\ \nabla_{\phi_{bc}} H_{bc} \end{bmatrix}}_{\nabla_{x_{bc}} H_{bc}} + \underbrace{\begin{bmatrix} 0 \\ 1 \end{bmatrix}}_{g(x_{bc})} v_{pv}, \\ y_{bc} = g^T(x_{bc}) \nabla_{x_{bc}} H_{bc} = i_{bc}, \end{cases} \quad (48)$$

where $\mathcal{R}(x_{bc}) = \text{diag}((1/R_L), 0)$, and $\mathcal{F}_{x_{bc}}$ is a skew-symmetric matrix with the form

$$\mathcal{F}_{x_{bc}} = \begin{bmatrix} 0 & S_{bc} \\ -S_{bc} & 0 \end{bmatrix}. \quad (49)$$

Based on the dynamics of (47) with its input-output port pair $(u_{bc}, y_{bc}) = (v_{pv}, i_{bc})$ and the Hamiltonian (46), and since $R_L > 0$, the power balance (9) clearly holds.

The following subsection provides the resulting interconnected system containing the PV cell and the DC-DC boost converter.

3.4. A PV Cell Array and the Boost Converter: An Energy-Based Approach. Based now on the pH formulation of the PV cell modelling approach (39) with Hamiltonian (35), and the DC-DC boost converter (47) with Hamiltonian (46), we are able to interconnect both stages in a single pH framework called Σ . The resulting system is

$$\Sigma \begin{cases} \underbrace{\begin{bmatrix} \dot{q}_{pv} \\ \dot{\phi}_{pv} \\ \dot{q}_{bc} \\ \dot{\phi}_{bc} \end{bmatrix}}_{\dot{x}} = \underbrace{\begin{bmatrix} -\frac{1}{R_p + R_s} & -1 & 0 & -1 \\ 1 & 0 & 0 & 0 \\ 0 & 0 & -\frac{1}{R_L} & S_{bc} \\ 1 & 0 & -S_{bc} & 0 \end{bmatrix}}_{\mathcal{F}(x) - \mathcal{R}(x)} \underbrace{\begin{bmatrix} \nabla_{q_{pv}} H \\ \nabla_{\phi_{pv}} H \\ \nabla_{q_{bc}} H \\ \nabla_{\phi_{bc}} H \end{bmatrix}}_{\nabla_x H} + \underbrace{\begin{bmatrix} \frac{R_p}{R_p + R_s} \\ 0 \\ 0 \\ 0 \end{bmatrix}}_{g(x)} i_s, \\ y_I = g^T(x) \nabla_x H = v_p, \end{cases} \quad (50)$$

where $\mathcal{F} = \text{diag}(\mathcal{F}_{x_{pv}}, \mathcal{F}_{x_{bc}})$, and $\mathcal{D} = \text{diag}(\mathcal{D}_{x_{pv}}, \mathcal{D}_{x_{bc}})$. The resulting system (49) has an input-output port pair $(u, y) = (i_s, v_p)$, and a Hamiltonian function

$$\begin{aligned} H(x) &= H_{pv}(q_{pv}, \phi_{pv}) + H_{bc}(q_{bc}, \phi_{bc}) \\ &= \frac{1}{2C_{pv}} q_{pv}^2 + \frac{1}{2C_{bc}} q_{bc}^2 + \frac{1}{2L_{bc}} \phi_{bc}^2. \end{aligned} \quad (51)$$

Clearly, the power balance (9) also holds for (49) since $\mathcal{R}(x) > 0$. In the follow-up, we presented our passivity-based control design to the MPPT problem. Furthermore, we compared its performance with respect to an SMC strategy previously introduced in Section 2.3. We finally support our main findings with simulation results in Section 5, together with experimental results in Section 6.

4. Proposed Control Approach

We have formulated in Section 2.3 a specific type of SMC strategy for our PV cell plus the DC-DC boost converter system for the MPPT problem according to [8, 12]. Now, we introduce our novel IDA-PBC design to the interconnected system (49), and the Hamiltonian function (50). Our IDA-PBC strategy is inspired by the work of [10, 35, 36], whose main design steps are recapitulated in Section 2.2.

First, we develop the IDA-PBC method of Section 2.2 to the interconnected pH system Σ as in (49). The feedback function $\beta(x)$ in (10) is obtained in order to control the system (49). We compute below the requirements on structure preservation (14), integrability (15), equilibrium assignment (16), and Lyapunov stability (17) [label = ()].

4.1. Structure Preservation. From Proposition 2, we assume that the matrix $J_a(x)$ is equal to zero which then reduces (11) in terms of $\mathcal{F}(x, \beta(x))$, $\mathcal{R}(x)$, $g(x)$, $R_a(x)$, and $\mathcal{K}(x)$, such that

$$\begin{aligned} \{[\mathcal{F}(x, \beta(x))] - [\mathcal{R}(x) + \mathcal{R}_a(x)]\} \mathcal{K}(x) \\ = -[\mathcal{R}_a(x)] \nabla_x H(x) + g(x, \beta(x)), \end{aligned} \quad (52)$$

where $g(x, \beta(x)) = g(x) i_s$, with i_s being the input of the system (50). Furthermore, $R_a(x)$ is assumed as

$$\mathcal{R}_a = \begin{bmatrix} 1 - \frac{1}{R_p + R_s} & 0 & 0 & 0 & 0 \\ 0 & 0 & 0 & 0 & 0 \\ 0 & 0 & 1 - \frac{1}{R_L} & 0 & 0 \\ 0 & 0 & 0 & 0 & 0 \end{bmatrix}. \quad (53)$$

Since we assume $[\mathcal{F}(x, \beta(x))] - [\mathcal{R}(x) + \mathcal{R}_a(x)]$ to be invertible, then the matrix $\mathcal{K}(x)$ in (52) is solved as

$$\mathcal{K}(x) = \begin{bmatrix} 0 \\ \frac{R_{p,s} - 1}{R_{p,s}} \frac{q_{pv}}{C_{pv}} + \frac{R_p}{R_{p,s}} i_s - \frac{R_L - 1}{\beta(x) R_L} \frac{q_{bc}}{C_{bc}} \\ 0 \\ \frac{R_L - 1}{\beta(x) R_L} \frac{q_{bc}}{C_{bc}} \end{bmatrix}, \quad (54)$$

where $R_{p,s} = R_p + R_s$. The form of the vector function $\mathcal{K}(x)$ in (54) guarantees that the closed-loop system (13) has structure preservation properties.

4.2. Integrability. The condition (15) is computed with the $\mathcal{K}(x)$ obtained on (54). Since i_s is a function of q_{pv} , as defined in (24), (26), and (25), and assuming that $R_s i_{pv}$ (the voltage in the serial equivalent resistor R_s) is very low with respect to v_{pv} , one solution for the vector $\mathcal{K}(x)$ comes from the differentiation of a scalar, which holds

$$\begin{aligned} \nabla_{q_{pv}} K &= 0, \\ \frac{R_{p,s} - 1}{R_{p,s} C_{pv}} - \frac{R_p i_0}{R_{p,s} C_{pv} n V_t} \exp\left(\frac{q_{pv}}{C_{pv} n V_t}\right) \\ - \frac{R_L - 1}{R_L} \frac{q_{bc}}{C_{bc}} \frac{\nabla_{q_{pv}} \beta(q_{pv})}{\beta(q_{pv})^2} &= 0. \end{aligned} \quad (55)$$

In Section 3, it is mentioned that $v_{pv} = q_{pv}/C_{pv}$ and $v_{bc} = q_{bc}/C_{bc}$. Given the structure preservation's result in (52), a solution to the PDE in (55) is

$$\beta(q_{pv}) = \frac{-(R_L - 1/R_L) v_{bc}}{C_1 - (R_{p,s} - 1/R_{p,s}) v_{pv} - (R_p/R_{p,s}) i_0 \exp(v_{pv}/nV_t)}. \quad (56)$$

C_1 in (56) is a term to be defined to accomplish the equilibrium assignment and Lyapunov stability forward. Equation (56) meets the requirement on (52) and complies the integrability condition.

4.3. Equilibrium Assignment at Stable Equilibrium x^* . From (51), it can be determined that

$$\nabla_x H(q_{pv}^*, \phi_{pv}^*, q_{bc}^*, \phi_{bc}^*) = \text{col}\left[\frac{q_{pv}^*}{C_{pv}}, 0, \frac{q_{bc}^*}{C_{bc}}, \frac{\phi_{bc}^*}{L_{cb}}\right], \quad (57)$$

where $(q_{pv}^*, \phi_{pv}^*, q_{bc}^*, \phi_{bc}^*)$ represent the equilibrium state of the system in (50). Thus, by equalizing (57) and (54) at the equilibrium state, it follows that

$$\frac{R_{p,s} - 1}{R_{p,s}} \frac{q_{pv}^*}{C_{pv}} + \frac{R_p}{R_{p,s}} i_s - \frac{R_L - 1}{\beta(x) R_L} \frac{q_{bc}^*}{C_{bc}} = 0. \quad (58)$$

We finally replace (56) in (58) to solve C_1 to comply with the equilibrium assignment. In this case, it is found two expressions that satisfy the solution. We have labeled such expressions as C_{1A} and C_{1B} which are

$$C_{1A} = \left(\frac{2(R_{p,s} - 1)}{R_{p,s}} \right) v_{pv}^* + \frac{R_p}{R_{p,s}} (i_{ph} + i_0), \quad (59)$$

$$C_{1B} = \left(\frac{-2R_p R_s}{R_p^2 - R_s^2} \right) v_{pv}^* + \frac{R_p}{R_{p,s}} i_0 \exp \left(\frac{v_{pv}^*}{n V_t} \right).$$

Notice how C_{1B} in (59) depends on the equilibrium state v_{pv}^* , which also depends on i_{ph} and G_{sun} .

4.4. Lyapunov Stability. Given the vector functions $\mathcal{K}(x)$ in (54) and $\nabla_x H(x^*)$ in (57), the Lyapunov stability condition in (17) is reduced to

$$0 > - \left(\frac{1}{C_{pv}} + \frac{1}{C_{bc}} + \frac{1}{L_{bc}} \right). \quad (60)$$

The inequality (60) meets the stability statement, leading the system to satisfy the MPP in the equilibrium trajectory described in (44).

4.5. IDA-PBC Control Law. The converter can be considered as a lossless stage controlled by the discrete set $S_{bc} = \{0, 1\}$, as introduced by [47]. Each element of S_{bc} represents a *mode*, where the exerted control law $\beta(q_p)$ over the switch in Figure 2 drives the state of S_{bc} on a mode 0 or 1, adjusting the controller to the desired trajectory of the MPP. The trajectory follows the solar irradiance G_{sun} , requiring a feedback reference to adjust the switching to a *threshold dynamic level*. Furthermore, to define this dynamic threshold level, the scalar function $\beta(q_{pv})$ is evaluated on the desired equilibrium point over the MPP trajectory, i.e., $\beta(q_{pv}^*)$, with q_{pv}^* as the state value that reaches the MPP. Notice how the voltage at the desired MPP depends also on the charge, i.e., $v_{pv}^* = q_{pv}^*/C_{pv}$ as in (44). In addition to this, the current i_{ph} as in (25) depends on the solar irradiance, then $\beta(q_{pv}^*)$ becomes a control parameter dynamically adjusted by the radiation power.

We finally define our main control law in the following proposition and remark.

Proposition 3. *Main result given a PV cell connected to a DC-DC boost converter represented in the pH system (50), with a duty cycle for the switch S_{bc} that lies between two modes, such that $0 \leq S_{bc} \leq 1$, as in [8], then the MPPT control*

TABLE 1: Key parameters for simulation and control.

Parameter description	Magnitude
Environment temperature T	30
PV cell temperature T_v	30
PV nominal irradiation G_{nom}	1000 kW/m ²
PV cell output short circuit $I_{SC,nom}^a$	1.95 A
PV cell output open circuit $V_{OC,nom}^a$	6.5 V
PV cell output $I_{nom}@MPPa$	1.42 A
PV cell output $V_{nom}@MPP^a$	4.0 V
Saturation current i_0^b	745 μ A
Simplified constant a^b	0.711 V
PV cell series resistor R_s^b	43m Ω
PV cell shunt resistor R_p^b	11.28 Ω
PV cell DC-link capacitor C_{pv}	470 μ F
DC-DC boost capacitor C_{bc}	14.1 mF
DC-DC boost inductor L_{bc}	2 mH

^aObtained experimentally @ G_{nom} as in Figure 8. ^bCalculated from [49].

objective is obtained via a scalar function $\beta(x)$ in (56) which solves the PDE in (11). Inspired by [12, 47], the proposed control signal is given by

$$S_{bc} = \begin{cases} 1 & \text{for } \beta(q_{pv}) - \beta(q_{pv}^*) > 0 \\ 0 & \text{for } \beta(q_{pv}) - \beta(q_{pv}^*) \leq 0, \end{cases} \quad (61)$$

following that $\beta(q_{pv}) - \beta(q_{pv}^)$ works as an error tracking control, where $\beta(q_{pv}^*)$ is constantly adjusted by the state variables at the equilibrium point of the system as a dynamic threshold level that follows the MPPT trajectory.*

Proof. The closed-loop pH system in (13) has a Hamiltonian function $H_d(x, \beta(x))$ given by

$$H_d(x, \beta(x)) = H_I(x, \beta(x)) + H_a(x, \beta(x)), \quad (62)$$

with $H_I(x, \beta(x))$ defined in (51) and $H_a(x, \beta(x))$ being the energy of the desired controller. Hence, for the given $\beta(x)$, $\mathcal{F}(x, \beta(x))$, and $\mathcal{R}(x)$, the solution of (52) is a gradient of the form

$$\mathcal{K}(x) = \nabla_x H_a(x, \beta(x)) \quad (63)$$

if and only if the integrability condition (16) is satisfied. We have demonstrated that $H_d(x, \beta(x))$ is a Lyapunov candidate. Furthermore, the system (14) reaches stability at the equilibrium point x^* on (45) over the MPP trajectory: firstly, the equilibrium assignment condition on (60) showed that the function $H_d(x, \beta(x))$ has an isolated extremum at x^* , since it is solved to satisfy (17); secondly, the Lyapunov stability condition (61) proved that it is an isolated minimum of the function. \square

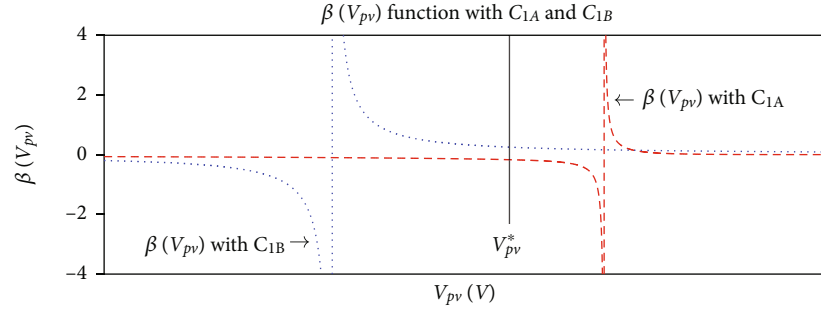
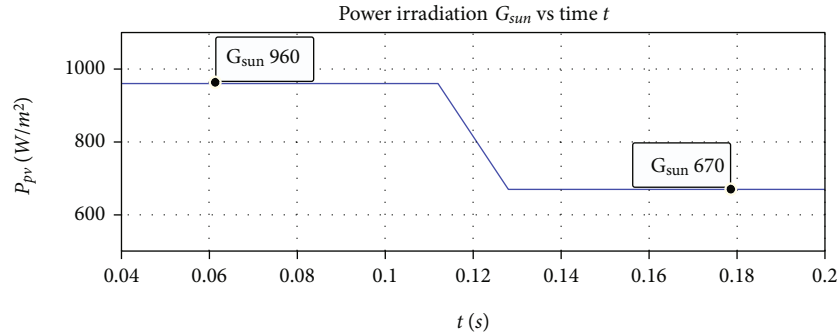
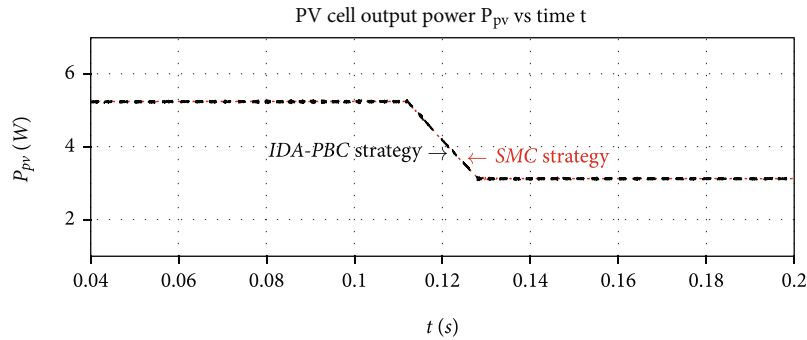


FIGURE 3: Behaviour of the function $\beta(v_{pv})$ for the constants C_{1A} (dashed red line) and C_{1B} (dot blue line).



(a) Input power radiation step given by $G_{\text{sun}} = 960 \text{ W/m}^2$ for the time interval $(0.040, 0.112) \text{ s}$ and $G_{\text{sun}} = 670 \text{ W/m}^2$ for the time interval $(0.128, 0.200) \text{ s}$ (blue solid line)



(b) PV cell output power response P_{pv} with IDA-PBC strategy (dark dashed line) and PV cell output power response P_{pv} with SMC strategy (red dot line).

All measurements are done with a fixed load of $R_L = 10\Omega$

FIGURE 4: PV cell output power response to given input power radiation levels with IDA-PBC and SMC strategies.

In the following section, we compare the performance of our IDA-PBC control law (62) with the SMC strategy of Section 2.3 via numerical simulations and an experimental setup.

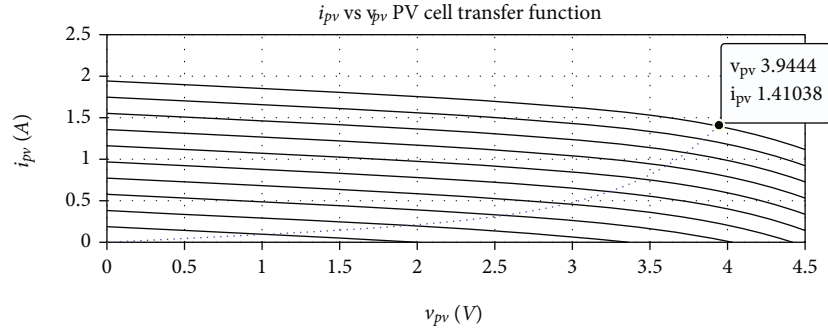
5. Simulation Results

We simulate here the behaviour of the terms C_{1A} and C_{1B} from the control function $\beta(v_{pv})$, the transfer and power functions of the PV cell, and the response of the PV cell output power at different solar irradiance and output impedance levels. The simulation integrates the control action of our IDA-PBC and the SMC strategies over the pH system (50). Then, a behavioural multi-physics numerical model is developed, fed with the key parameters of Table 1 from Sec-

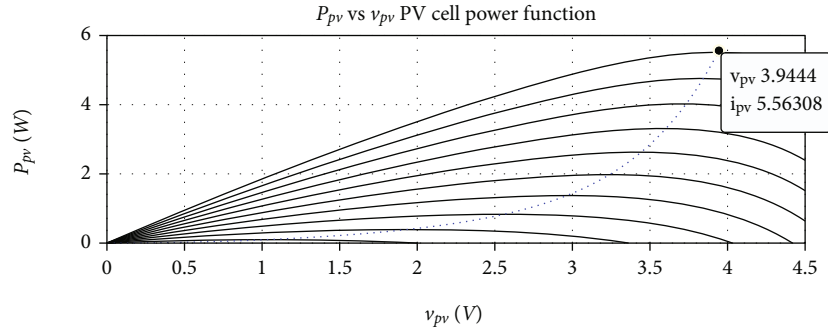
tion 6. In order to get accurate simulation results, the sampling of the states for the control strategies ($\{v_{pv}, G_{\text{sun}}\}$ in IDA-PBC and $\{v_{pv}, i_{pv}\}$ in SMC) is restricted in frequency into the programming code.

From (56) and (59), it can be demonstrated that the function $\beta(v_{pv})$ has a *discontinuous behaviour* at the right and left sides of a given equilibrium state v_{pv}^* , respectively, in terms of C_{1A} and C_{1B} , as shown in Figure 3. Therefore, C_{1A} must be applied to the control law (61) when the instant value of $v_{pv} \leq v_{pv}^*$ and C_{1B} in the case $v_{pv} > v_{pv}^*$ to ensure the continuity of the control law over the whole tracking trajectory.

In Figure 4, the responses of the PV cell output power P_{pv} for the strategies IDA-PBC and SMC in (b) are



(a) PV cell transfer function at input solar irradiance levels (solid black lines); maximum power impedance function at MPP (blue dot line)



(b) PV cell output power function P_{pv} at input solar irradiance levels (solid black lines); maximum power point trajectory (blue dot line)

FIGURE 5: The PV cell's transfer and output power functions at several input solar irradiance levels.

compared under *level changes on the solar irradiance* as shown in (a), from 960 W/m^2 to 670 W/m^2 . Here, the PV cell's output power P_{pv} of both the IDA-PBC as in (61), and the SMC as in (23), shows no perceptible differences. The sample rate of the simulation for both control strategies is set to 10 MHz, in order to ensure an SMC suitable performance due to the extra-computation requirements for the differential equation calculation.

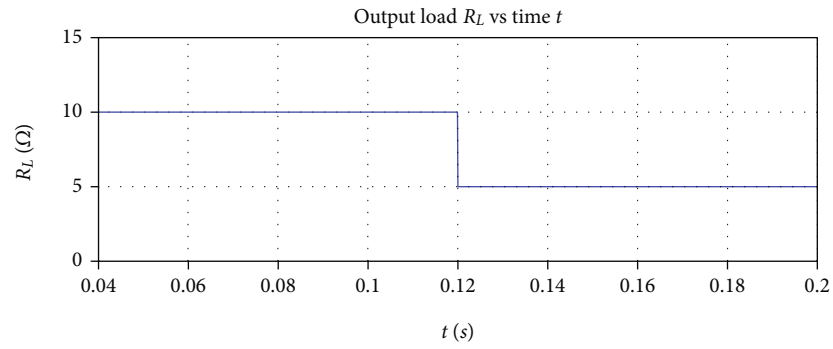
In Figure 5, we show the *transfer functions* i_{pv} vs v_{pv} in (a) and P_{pv} vs v_{pv} in (b) of a PV cell, in order to determine the MPP of the array. Such characteristic curves of the PV cell are based on the dynamics of (26) to (28), with the key parameters given in Table 1. The figure also shows the values of v_{pv} , i_{pv} , and P_{pv} at the MPP for a solar irradiance $G_{\text{sun}} = 1000$. We test and evaluate here the capacity of the control laws (61) and (23) to follow the PV cell functions' behaviour.

In order to further compare the performance of the IDA-PBC and the SMC strategies, the DC-DC boost converter load R_L is simulated as a time function, following a *step perturbation* from 10Ω to 5Ω (Figure 6(a)). As a result, the power signal P_{pv} remains unmovable for both the IDA-PBC and the SMC (Figure 6(b)). Once again, the sample rate of the simulation for both control strategies is set to 10 MHz, due to the extra-computation requirements for the differential equation calculation required by the SMC.

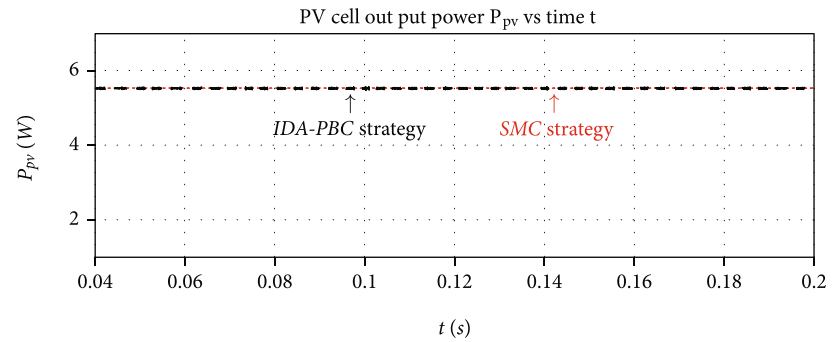
The radiation is represented by 100 W/m^2 steps from 100 to 1000 W/m^2 for both (a) and (b).

6. Experimental Results

The experimental setup used to measure the radiation and control of the MPP is shown in Figure 7. The setup consists of (a) commercial PV cell JD-7 W; (b) an open-source electronic prototyping platform Arduino UNO; (c) an Adafruit data logger shield; (d) irradiance sensor Spectrum 210; (e) hall current sensor module ACS712 5A; (f) multimeter BK Precision 393; (g) oscilloscope BK Precision 2540C; (h) laptop DELL Latitude 5491; (i) generic electronic components (resistors, capacitors, inductors, semiconductors); (j) protective boxes [48]. We have used real-time data from a sensor of the Costa Rican's National Meteorological Institute (<https://www.imn.ac.cr/web/imn/inicio>), to calibrate our irradiance sensor Spectrum323 210. The experimental set up from Figure 7 allows to track the physical parameters v_{pv} and i_{pv} under constant solar irradiance of $\approx 1000 \text{ W/m}^2$, $\approx 850 \text{ W/m}^2$, and $\approx 700 \text{ W/m}^2$. Meanwhile, a variable resistance load connected at the output of the PV cell induced different impedance matching conditions. Hence, the *experimental PV cell output power function* was determined by fitting the PV cell output power P_{pv} at the MPP, as shown in Figure 8. An MPP is determined from the experimental data for $P_{pv} \approx 5.7 \text{ W}$ when the voltage $v_{pv} \approx 4.0 \text{ V}$ and $i_{pv} \approx 1.41 \text{ A}$. In addition to this, the values $I_{SC, \text{nom}} \approx 1.95 \text{ A}$ and $V_{OC, \text{nom}} \approx 6.5 \text{ V}$ are calculated at the top end and bottom end of the impedance matching. These aforementioned parameters allow the *characterization of the PV cell* as explained in the follow-up.



(a) R_L step from 10Ω to 5Ω at $t = 0.12$ s under the constant input solar irradiance $G_{Sun} = 1000$ W/m² (blue solid line)



(b) PV cell output power response P_{pv} with IDA-PBC strategy (dark dashed line) and PV cell output power response P_{pv} with SMC strategy (red dot line)

FIGURE 6: PV cell output power response to given output load levels with IDA-PBC and SMC strategies.

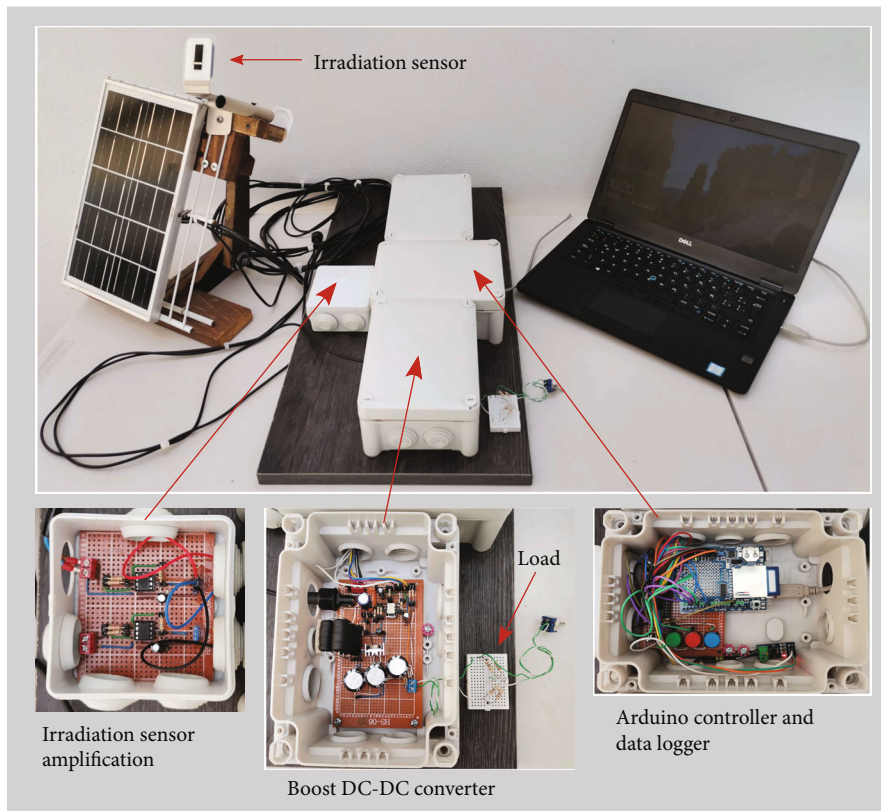


FIGURE 7: Experimental setup for radiation measurements and implementation of the control strategy.

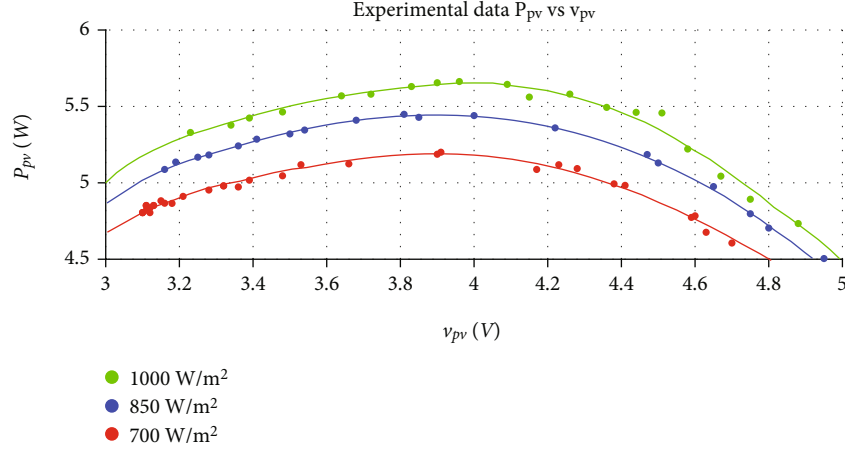


FIGURE 8: Experimental measurement of the PV cell output power function P_{pv} vs input solar irradiance G_{Sun} .

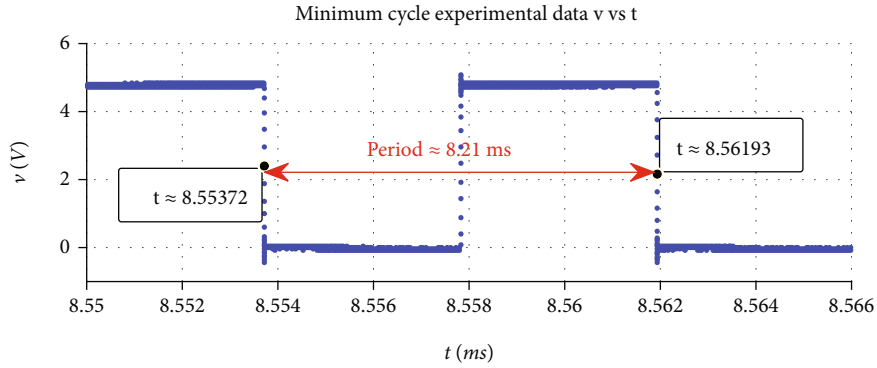


FIGURE 9: Minimum period of sampling cycle of the IDA-PBC strategy, due to the computing capacities of the hardware platform.

In order to get key constants from a real PV cell for simulation and experimental purposes, the modelling approach of (24) to (28) is simplified to evaluate the current i_{pv} . The simplification follows the guidelines of [49] which means that

$$i_{pv} = i_{ph} - i_0 \left(\exp \left(\frac{v_{pv} + i_{pv} R_s}{a} \right) - 1 \right) - \frac{v_{pv} + i_{pv} R_s}{R_p}, \quad (64)$$

where $a = nV_t$ and i_0 are considered as constant values. Hence, the physical parameters are calculated from the data in Figure 8. Such parameters measured from the PV cell allow defining the key constants for (64), following the procedure of [49]. In Table 1, we provide a summary of the obtained values of the key constants and parameters, together with the parameters of the DC-DC boost converter.

We evaluate here the *frequency performance* of the switch S_{bc} in the boost DC-DC converter governed under the IDA-PBC strategy and implemented in the hardware platform. A square signal, whose duty cycle is determined by the IDA-PCB code delay, is applied to execute a change of state on the switch S_{bc} . A change of state in the signal sent from the controller to the switch allows calculating the maximum frequency that the hardware platform can deliver. It follows that the maximum frequency of the switch with the

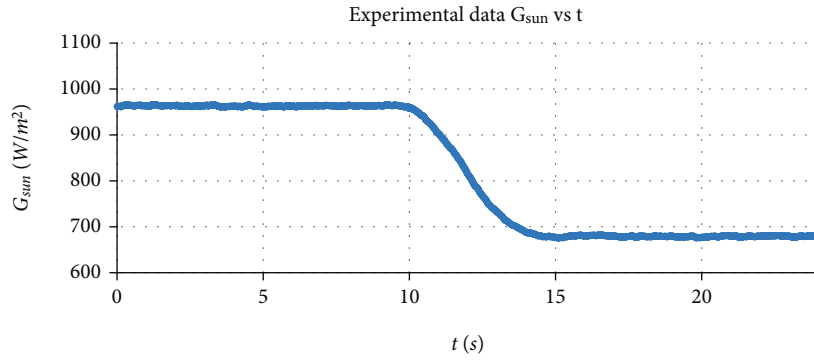
IDA-PBC strategy is approximately 122 Hz (period of 8.21 ms), as shown in Figure 9. Moreover, based on [50], the dynamic power dissipated on the digital circuit's clock cycle signals can be determined as

$$P = ACV^2 F, \quad (65)$$

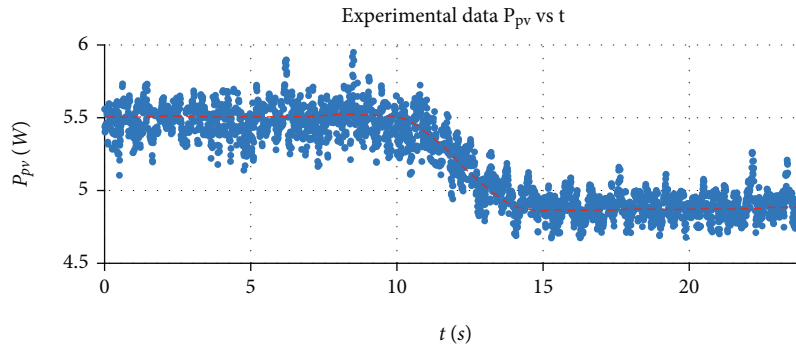
where A is the activity factor of the switching, C is the equivalent capacitance of the circuit, V is the source voltage applied across the circuit, and F is the switching frequency. Hence, from (65) it can be considered that the dynamic power of the boost DC-DC converter circuitry reduces according to the magnitude of switching frequency F .

In order to evaluate the response of IDA-PBC strategy, the system setup in Figure 7 is firstly exposed to a constant solar irradiance. Then, the PV cell device is rotated, generating an *irradiance step* from $G_{Sun} \approx 960 \text{ W/m}^2$ to $G_{Sun} \approx 670 \text{ W/m}^2$, as shown in Figure 10(a). Consistently, the response of the output power P_{pv} to this irradiance step is measured. It is experimentally demonstrated that the IDA-PBC strategy implemented into the hardware platform tracks the MPP (Figure 10(b)), according to the P_{pv} experimental trend lines of Figure 8.

Finally, Figure 11(a) shows an output *impedance step* from 10Ω to 5Ω that is induced at the output of the boost

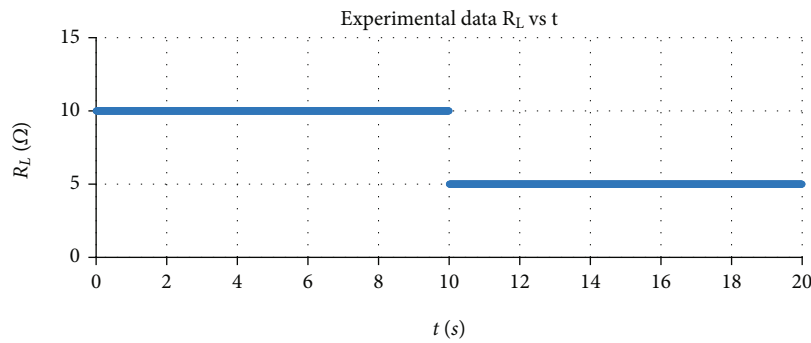


(a) Input power radiation step given by $G_{\text{sun}} \approx 960 \text{ W/m}^2$ for the time interval (0, 10) s and $G_{\text{sun}} \approx 670 \text{ W/m}^2$ for the time interval (15, 25) s

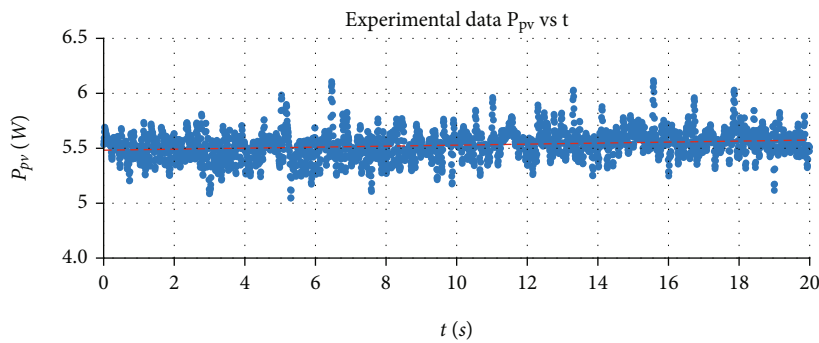


(b) PV cell output power response P_{pv} with the IDA-PBC strategy

FIGURE 10: Experimental data of the PV cell output power response to a given input power radiation with the IDA-PBC strategy implemented into a hardware platform.



(a)



(b)

FIGURE 11: Experimental data of the PV cell output power response to a given step of the output load at a constant sun irradiation power $G_{\text{sun}} \approx 970 \text{ W/m}^2$, with the IDA-PBC strategy implemented into a hardware platform. (a) R_L step from 10Ω to 5Ω at $t = 10$ s. (b) PV cell output power response P_{pv} with the IDA-PBC strategy.

DC-DC converter at a constant solar irradiance of $G_{\text{Sun}} \approx 960 \text{ W/m}^2$. Once again, the implemented IDA-PBC strategy controls the system and keeps the PV cell output power P_{pv} unmovable around 5.5 W (Figure 11(b)). Such result is consistent with the MPP reported on the P_{pv} experimental functions of Figure 8.

Remark 4. The proposed IDA-PBC requires to monitor the PV cell output voltage v_p and the radiation power G_{Sun} as input parameters. Such strategy is a noninvasive approach since it operates without electrical current sensors, contrary to the SMC law in (22) and the IDA-PBC law of [10] that require to monitor electrical currents at the output of the PV cell.

7. Concluding Remarks and Future Work

We have proposed a novel control law for the local MPPT problem in an energy-based setting, which takes advantage of the structure preservation properties of the system under study. The simplicity in the calculations allows an adequate response under uncertainties in radiation inputs. We have also simulation results on an SMC control law strategy. Our novel control law and the SMC are simulated, and we demonstrated that both strategies are able to reach the addressed MPPT problem. However, for the physical implementation, our IDA-PBC approach requires no direct electrical current measurements, being, in this case, less invasive and requiring less monitoring sensors than the SMC strategy.

The control strategy is tested for a single PV cell's MPPT. However, the solution can be extended to applications where PS is not critical. For instance, an application with PV cell arrays governed with separated DC-DC converters, exposed to the same radiation level or localized far away from PS sources. It means that several PV cell arrays could be controlled with a single sensor. Since the sensor is externally connected, its installation does not depend on a specific place. Moreover, a single sensor requires a single connection line. Such installation simplicity reduces implementation costs, e.g., wiring over the array, in applications such as low power production PV farms and roof PV cell arrays.

The IDA-PBC strategy is physically implemented in a prototype governed by a hardware platform, with a maximum switching rate on the control signal of 122 Hz. The sense sampling time in our control strategy is faster than the SMC strategy. Such an advantage is due to the algorithm's simplicity, resulting in a low-cost implementation and a low dynamic-power consumption. Moreover, the PV cell is characterized to obtain the MPP at several solar irradiance inputs. The prototype's performance is tested by setting step changes in the dynamics of the system: firstly, in the solar irradiance input over the PV cell, and secondly, in the impedance output of the boost DC-DC converter. In both cases, the output power remains over the MPP of the PV cell, according to the characterization of the PV cell. Our control law requires the PV cell's parameter identifica-

tion. Such identification follows mainly from the manufacturer's datasheet. The parameter identification procedure should be made once if the PV array is homogeneous in terms of PV cells.

Future work will consider the design and implementation of the proposed control law in a higher power physical system and under reactive output loads conditions.

Data Availability

All the data that supports this research is available under request at the authors' email addresses.

Conflicts of Interest

The authors declare that there is no conflict of interest regarding the publication of this paper.

Acknowledgments

The authors thank the Instituto Tecnológico de Costa Rica (ITCR), Cartago, and the Centro Académico de Alajuela for providing the necessary infrastructure and resources to carry out this work.

References

- [1] M. K. H. Rabaia, M. A. Abdelkareem, E. T. Sayed et al., "Environmental impacts of solar energy systems: a review," *Science of the Total Environment*, vol. 754, article 141989, 2021.
- [2] S. D. Al-Majidi, M. F. Abbod, and H. S. Al-Raweshidy, "A novel maximum power point tracking technique based on fuzzy logic for photovoltaic systems," *International Journal of Hydrogen Energy*, vol. 43, no. 31, pp. 14158–14171, 2018.
- [3] R. N. Shaw, P. Walde, and A. Ghosh, "Iot based mppt for performance improvement of solar pv arrays operating under partial shade dispersion," in *2020 IEEE 9th Power India International Conference (PIICON)*, pp. 1–4, Sonapat, India, 2020.
- [4] B. Subudhi and R. Pradhan, "A comparative study on maximum power point tracking techniques for photo voltaic power systems," *IEEE Transactions on Sustainable Energy*, vol. 4, no. 1, pp. 89–98, 2012.
- [5] P. Bhatnagar and R. Nema, "Maximum power point tracking control techniques: State-of-the-art in photovoltaic applications," *Renewable and Sustainable Energy Reviews*, vol. 23, pp. 224–241, 2013.
- [6] M. A. Sameh, M. A. Badr, M. A. L. Badr, M. I. Marei, and M. A. Attia, "Optimized pia controller for photo voltaic system using hybrid particle swarm optimization and cuttlefish algorithms," in *2018 7th International Conference on Renewable Energy Research and Applications (ICRERA)*, pp. 1102–1108, Paris, France, 2018.
- [7] A. Kihal, F. Krim, A. Laib, B. Talbi, and H. Afghoul, "An improved MPPT scheme employing adaptive integral derivative sliding mode control for photovoltaic systems under fast irradiation changes," *ISA Transactions*, vol. 87, pp. 297–306, 2019.
- [8] C.-C. Chu and C.-L. Chen, "Robust maximum power point tracking method for photovoltaic cells: a sliding mode control approach," *Solar Energy*, vol. 83, no. 8, pp. 1370–1378, 2009.

- [9] N. Khefifi, A. Houari, M. Machmoum, and M. Ghanes, "Interconnection and damping assignment passivity for the control of pv/battery hybrid power source in islanded microgrid," *International Journal of Renewable Energy Research (IJRER)*, vol. 9, no. 4, pp. 1790–1802, 2019.
- [10] S. Pang, B. Nahid-Mobarakeh, S. Pierfederici et al., "Interconnection and damping assignment passivity-based control applied to on-board DC–DC power converter system supplying constant power load," *IEEE Transactions on Industry Applications*, vol. 55, no. 6, pp. 6476–6485, 2019.
- [11] N. Kasa, T. Iida, and L. Chen, "Flyback inverter controlled by sensorless current mppt for photovoltaic power system," *IEEE Transactions on Industrial Electronics*, vol. 52, no. 4, pp. 1145–1152, 2005.
- [12] A. Kchaou, A. Naamane, Y. Koubaa, and N. M'sirdi, "Second order sliding mode-based MPPT control for photovoltaic applications," *Solar Energy*, vol. 155, pp. 758–769, 2017.
- [13] L. Shang, H. Guo, and W. Zhu, "An improved mppt control strategy based on incremental conductance algorithm, Protection and Control of Modern Power Systems," *Protection and Control of Modern Power Systems*, vol. 5, no. 1, pp. 1–8, 2020.
- [14] S. Li, "A variable-weather-parameter MPPT control strategy based on MPPT constraint conditions of PV system with inverter," *Energy Conversion and Management*, vol. 197, article 111873, 2019.
- [15] H. Rezk, M. Aly, M. Al-Dhaifallah, and M. Shoyama, "Design and hardware implementation of new adaptive fuzzy logic-based MPPT control method for photovoltaic applications," *IEEE Access*, vol. 7, pp. 106427–106438, 2019.
- [16] Ž. Zečević and M. Rolevski, "Neural network approach to MPPT control and irradiance estimation," *Applied Sciences*, vol. 10, no. 15, 2020.
- [17] M. A. Sameh, M. A. Badr, M. I. Mare, and M. A. Attia, "Enhancing the performance of photovoltaic systems under partial shading conditions using cuttlefish algorithm," in *2019 8th International Conference on Renewable Energy Research and Applications (ICRERA)*, pp. 874–885, Brasov, Romania, 2019.
- [18] A. E. Mohamed, M. I. Marei, and W. El-khattam, "A maximum power point tracking technique for pv under partial shading condition," in *2018 8th IEEE India International Conference on Power Electronics (IICPE)*, pp. 1–6, Jaipur, India, 2018.
- [19] Z. M. Ali, N. Vu Quynh, S. Dadfar, and H. Nakamura, "Variable step size perturb and observe MPPT controller by applying θ -modified krill herd algorithm-sliding mode controller under partially shaded conditions," *Journal of Cleaner Production*, vol. 271, article 122243, 2020.
- [20] R. Ramaprabha, M. Balaji, and B. Mathur, "Maximum power point tracking of partially shaded solar PV system using modified Fibonacci search method with fuzzy controller," *International Journal of Electrical Power & Energy Systems*, vol. 43, no. 1, pp. 754–765, 2012.
- [21] M. Mansoor, A. F. Mirza, and Q. Ling, "Harris hawk optimization-based MPPT control for PV systems under partial shading conditions," *Journal of Cleaner Production*, vol. 274, article 122857, 2020.
- [22] M. H. Zafar, T. Al-shahrani, N. M. Khan et al., "Group teaching optimization algorithm based MPPT control of PV systems under partial shading and complex partial shading," *Electronics*, vol. 9, no. 11, 2020.
- [23] M. Hamza Zafar, N. Mujeeb Khan, A. Feroz Mirza et al., "A novel meta-heuristic optimization algorithm based MPPT control technique for PV systems under complex partial shading condition," *Sustainable Energy Technologies and Assessments*, vol. 47, article 101367, 2021.
- [24] M. Mansoor, A. F. Mirza, F. Long, and Q. Ling, "An intelligent tunicate swarm algorithm based MPPT control strategy for multiple configurations of PV systems under partial shading conditions," *Advanced Theory and Simulations*, vol. 4, no. 12, article 2100246, 2021.
- [25] M. Joisher, D. Singh, S. Taheri, D. R. Espinoza-Trejo, E. Pouresmaeil, and H. Taheri, "A hybrid evolutionary based MPPT for photovoltaic systems under partial shading conditions," *IEEE Access*, vol. 8, pp. 38481–38492, 2020.
- [26] H. Li, D. Yang, W. Su, J. Lu, and X. Yu, "An overall distribution particle swarm optimization MPPT algorithm for photovoltaic system under partial shading," *IEEE Transactions on Industrial Electronics*, vol. 66, no. 1, pp. 265–275, 2019.
- [27] R. Ortega, J. Perez, P. Nicklasson, and H. Sira-Ramirez, *Passivity-Based Control of Euler-Lagrange Systems: Mechanical, Electrical and Electromechanical Applications*, Springer, London, 2013.
- [28] A. Achour, D. Rekioua, A. Mohammedi, Z. Mokrani, T. Rekioua, and S. Bacha, "Application of direct torque control to a photovoltaic pumping system with sliding-mode control optimization," *Electric Power Components and Systems*, vol. 44, no. 2, pp. 172–184, 2016.
- [29] Z. Xin, H. Li, Q. Liu, and P. C. Loh, "A review of megahertz current sensors for megahertz power converters," *IEEE Transactions on Power Electronics*, vol. 37, no. 6, pp. 6720–6738, 2022.
- [30] P. Ripka, "Electric current sensors: a review," *Measurement Science and Technology*, vol. 21, no. 11, article 112001, 2010.
- [31] P. S. Samrat, F. F. Edwin, and W. Xiao, "Review of current sensorless maximum power point tracking technologies for photovoltaic power systems," in *2013 International Conference on Renewable Energy Research and Applications (ICRERA)*, pp. 862–867, Madrid, Spain, 2013.
- [32] R. Ortega, J. G. Romero, P. Borja, and A. Donaire, *PID Passivity-Based Control of Nonlinear Systems with Applications*, John Wiley & Sons, 2021.
- [33] A. Van Der Schaft and D. Jeltsema, "Port-Hamiltonian systems theory: an introductory overview," *Foundations and Trends® in Systems and Control*, vol. 1, no. 2, pp. 173–378, 2014.
- [34] V. Duindam, A. Macchelli, S. Stramigioli, and H. Bruyninckx, *Modeling and Control of Complex Physical Systems: The Port-Hamiltonian Approach*, Springer, Berlin, Germany, 2009.
- [35] R. Ortega and E. GarcAa-Canseco, "Interconnection and damping assignment passivity-based control: a survey," *European Journal of Control*, vol. 10, no. 5, pp. 432–450, 2004.
- [36] R. Ortega, A. van der Schaft, B. Maschke, and G. Escobar, "Interconnection and damping assignment passivity-based control of port- controlled Hamiltonian systems," *Automatica*, vol. 38, no. 4, pp. 585–596, 2002.
- [37] Y. Belkhier, R. N. Shaw, M. Bures et al., "Robust interconnection and damping assignment energy-based control for a permanent magnet synchronous motor using high order sliding mode approach and nonlinear observer," *Energy Reports*, vol. 8, pp. 1731–1740, 2022.

- [38] H. Phillips-Brenes, R. Pereira-Arroyo, and M. Munoz-Arias, "Energy-based model of a solar-powered pumped-hydro storage system, in 2019," in *2019 IEEE 39th Central America and Panama Convention (CONCAPAN XXXIX)*, pp. 1–6, Guatemala City, Guatemala, 2019.
- [39] M. F. N. Khan, G. Ali, and A. K. Khan, "A review of estimating solar photovoltaic cell parameters," in *2019 2nd International Conference on Computing, Mathematics and Engineering Technologies (iCoMET)*, pp. 1–6, Sukkur, Pakistan, 2019.
- [40] P. J. Gnetchejo, S. N. Essiane, P. Ele, R. Wamkeue, D. M. Wapet, and S. P. Ngoffe, "Important notes on parameter estimation of solar photovoltaic cell," *Energy Conversion and Management*, vol. 197, article 111870, 2019.
- [41] Y. Chaibi, M. Salhi, A. El-jouni, and A. Essadki, "A new method to extract the equivalent circuit parameters of a photovoltaic panel," *Solar Energy*, vol. 163, pp. 376–386, 2018.
- [42] F. F. Muhammad, A. W. Karim Sangawi, S. Hashim, S. K. Ghoshal, I. K. Abdullah, and S. S. Hameed, "Simple and efficient estimation of photovoltaic cells and modules parameters using approximation and correction technique," *PloS One*, vol. 14, no. 5, 2019.
- [43] V. Lo Brano, A. Orioli, G. Ciulla, and A. Di Gangi, "An improved five-parameter model for photovoltaic modules," *Solar Energy Materials and Solar Cells*, vol. 94, no. 8, 2010.
- [44] M. G. Villalva, J. R. Gazoli, and E. Ruppert Filho, "Comprehensive approach to modeling and simulation of photovoltaic arrays," *IEEE Transactions on Power Electronics*, vol. 24, no. 5, pp. 1198–1208, 2009.
- [45] P. Sanjeevikumar, G. Grandi, P. W. Wheeler, F. Blaabjerg, and J. Loncarski, "A simple mppt algorithm for novel pv power generation system by high output voltage dc-dc boost converter," in *2015 IEEE 24th International Symposium on Industrial Electronics (ISIE)*, pp. 214–220, Buzios, Brazil, 2015.
- [46] R. Kumar and B. Singh, "Buck-boost converter fed BLDC motor drive for solar PV array based water pumping," in *2014 IEEE International Conference on Power Electronics, Drives and Energy Systems (PEDES)*, pp. 1–6, Mumbai, India, 2014.
- [47] G. Escobar, A. J. van der Schaft, and R. Ortega, "A Hamiltonian viewpoint in the modeling of switching power converters," *Automatica*, vol. 35, no. 3, pp. 445–452, 1999.
- [48] "Spectron irradiance sensors 210, 320 & 485mb," <https://www.tritec-energy.com/wpcontent/uploads/2020/02/spektron-210-de.pdf>.
- [49] E. I. Batzelis and S. A. Papathanassiou, "A method for the analytical extraction of the single-diode PV model parameters," *IEEE Transactions on Sustainable Energy*, vol. 7, no. 2, pp. 504–512, 2016.
- [50] B. R. Gaster, L. Howes, D. R. Kaeli, P. Mistry, and D. Schaa, *Chapter 3 - OpenCL Device Architectures*, Morgan Kaufmann, Boston, MA, USA, 2nd edition, 2013.